

High-heat-flux performance limit of tungsten monoblock targets: Impact on the armor materials and implications for power exhaust capacity

Jeong-Ha You^{a,*}, Henri Greuner^a, Bernd Böswirth^a, Katja Hunger^a, Selanna Roccella^b, Helen Roche^c

^a Max Planck Institute for Plasma Physics, Boltzmannstr. 2, 85748 Garching, Germany

^b ENEA Frascati, Department of Fusion, via E. Fermi 45, 00044 Frascati, Italy

^c CEA, IRFM, F-13108 Saint Paul Lez Durance, France

ARTICLE INFO

Keywords:

DEMO
Divertor targets
Armor
High-heat-flux
Tungsten monoblock
Recrystallization

ABSTRACT

Development of a reliable high-heat-flux (HHF) technology is one of the crucial requirements of power exhaust strategy for a fusion reactor. The baseline HHF technology of the EU-DEMO, which inherited mostly the ITER technology, is based on the tungsten monoblock design and hot radial pressing joining technique. Thermal resilience and structural integrity under all off-normal transient events foreseen are essential prerequisites for validation of the technology towards the demonstration of full-scale prototype manufacture. Hence, the HHF performance of the baseline technology needs to be evaluated also in the transient overload regime. To this end, we conducted an extensive HHF testing campaign using small-scale test mock-ups of the tungsten monoblock target for two slow (10 s) overloads at 20 MW/m² (up to 2000 pulses) and 25 MW/m² (1000 pulses), and for a short (0.4 s) overload at 40 MW/m² (5000 pulses). Furthermore, excessive heat loads (32–37 MW/m²) were applied beyond the armor melting event to test the structural stability at limit loads. IR thermography, ultrasonic inspection and electron microscopy (EBSD) delivered direct information and insight on the structural integrity and the impact on the armor microstructure. It was found that the tungsten monoblock target remained fully intact at least up to 1000 heating cycles at 20 MW/m² (10 s) and survived 2000 cycles without any major failure. At 25 MW/m² (10 s), the mock-ups remained nearly intact at least up to 500 heating cycles and survived 1000 cycles without critical failure. However, the armor surface showed substantial deformation roughening with the height of 1000 μm after 1000 cycles. At 40 MW/m² with short pulses (0.4 s), the mock-ups remained fully intact without any serious damage at least up to 5000 cycles. The mock-ups even withstood the limit heat load of 32 MW/m² at least for a few pulses. Under excessive overloads (33–37 MW/m²) above the critical incident heat flux, armor melting preceded any other potential failures (e.g. pipe rupture by coolant boiling).

1. Introduction

The issue of power exhaust has been posing a serious challenge for the plasma physicists as well as for the engineers in the fusion reactor community [1–4]. Divertor is one of the key in-vessel components in charge of power exhaust. European demonstration reactor (EU-DEMO) with the power capacity of 2 GW foresees roughly 339 MW to be exhausted via the divertor where 122 MW thereof via the targets, mostly as surface heat flux by particles and radiation and partly as volumetric nuclear heating [5].

In the present article, the topic focuses on the heat removal capacity of the targets. Fig. 1 shows the CAD model of the outer vertical target of

the EU-DEMO as of 2020. Targets shall be subjected to a plasma footprint producing a poloidal heat flux profile with a Gaussian peaking at the narrow strike point. The strong concentration of heat flux at the strike point is a direct consequence of the diverted magnetic field configuration of the tokamak. The maximum heat flux density is predicted to reach roughly 10 MW/m² during the quasi-stationary normal operation and up to 20–40 MW/m² during off-normal transient events (e.g. plasma reattachment with strike point sweeping) [5]. The transient heat loads during the off-normal events presents a particular challenge for power exhaust. To cope with such excessive heat loads, a huge cooling capacity and thermal resilience at the strike point is mandatory. To this end, a lower operation temperature using ‘cold’ coolant

* Corresponding author.

E-mail address: you@ipp.mpg.de (J.-H. You).

<https://doi.org/10.1016/j.nme.2022.101307>

Received 23 August 2022; Received in revised form 2 November 2022; Accepted 11 November 2022

Available online 15 November 2022

2352-1791/© 2022 The Authors. Published by Elsevier Ltd. This is an open access article under the CC BY-NC-ND license (<http://creativecommons.org/licenses/by-nc-nd/4.0/>).

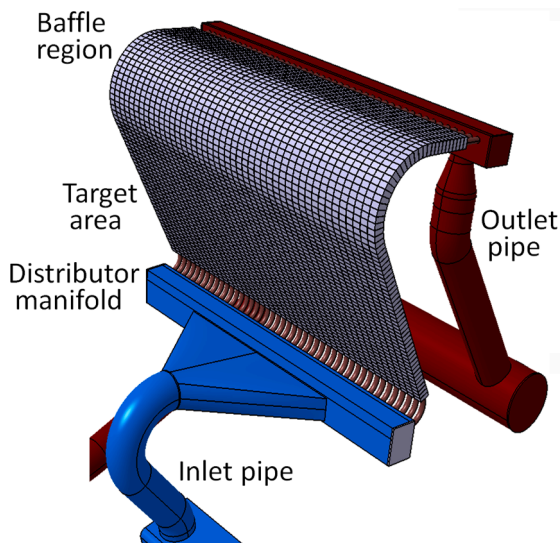


Fig. 1. CAD model of the outer vertical target of the EU-DEMO [5].

(≤ 150 °C) is ideally preferred [6–8]. On the other hand, under neutron irradiation, the materials undergo detrimental changes (e.g. embrittlement, reduced strength) due to transmutation and lattice damage [9–11]. Since lattice damages are favored at lower temperatures while recovered at higher temperatures, a higher operation temperature using ‘hot’ coolant (≥ 250 °C) would be beneficial. Such contradicting requirements imply that a prudent compromise is inevitable accepting the consequences of the trade-off [6,12]. The targets are supposed to survive for the specified lifetime of at least 1.5 full power year (fpy) [5]. Hence, mechanical stability of materials and structural integrity of the components remain crucial requirements.

Since 2014, the design and technology R&D activities for the EU-DEMO divertor have been conducted in the framework of the Work Package Divertor (WPDIV) of the EUROfusion Consortium. During the first funding period (2014–2020), preconceptual design studies and explorative technology R&D were conducted. One of the major R&D objectives was to optimize and qualify the baseline HHF technology. Extensive HHF testing campaigns were performed by means of neutral hydrogen beam or electron beam. Comprehensive characterizations were carried out with the help of infrared thermography, ultrasonic reflectometry and electron microscopy. In this article, an overview of the latest HHF testing campaign and post-mortem damage analysis is presented. The focus is placed on the overload tests (≥ 20 MW/m²) to address the ultimate HHF capacity of the baseline HHF technology.

2. Baseline HHF technology for the EU-DEMO targets

The baseline design concept of the EU-DEMO divertor target inherited mostly that of ITER (thus called ITER-like target) [13,14]. Its key features are:

- 1) Each target consists of a toroidal assembly of long target elements aligned in the poloidal direction (see Fig. 1).
- 2) Each target element consists of an axial array of rectangular tungsten armor blocks, which are joined to a water-cooled cooling pipe (CuCrZr alloy) running through the central bore of the blocks. Fig. 2 shows a small-scale mock-up of the target element.
- 3) A soft copper (OFHC) interlayer is inserted at the joining interface for relaxing stress. Fig. 3 displays two cut sections of the mock-up (a: quarter cross section, b: the interfacial region of the axial section).
- 4) Fig. 4 shows the technical drawings of a target element segment (a: lateral view, b: cross section). The cross section width is 23 mm (ITER target: 28 mm) and the armour thickness to the front face is 8

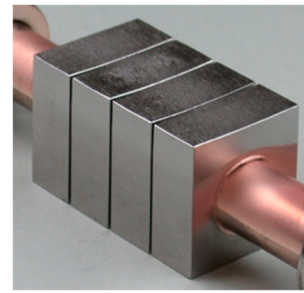


Fig. 2. Mock-up of a target element segment [14].

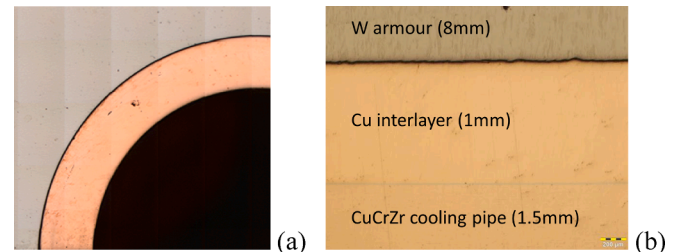


Fig. 3. Metallographic cut sections of the target element mock-up joined by HRP technique (a: a quarter cross section, b: axial section of the interfacial region) [14].

mm (ITER target: 7 mm). The reasoning for the modified dimensions are explained in [15–17]. The hydraulics design foresees a swirl tape inserted in the pipe to facilitate coolant turbulence.

The targets shall be cooled by pressurized water. The temperature and pressure of the coolant at the inlet of the target cooling circuit was set at 130 °C and 50 bar respectively. The local temperature and pressure of the coolant at the outlet point slightly deviates from the inlet condition (ΔT : +7 °C, Δp : –10 bar). The mean axial velocity of the coolant was set at 14 m/s (± 1 m/s). The minimum heat flux margin to the critical wall heat flux of nucleate boiling at the pipe wall reached ≥ 40 % (1.4) under stationary heat load of 20 MW/m². The computational verification of the cooling scheme is found elsewhere [5,18–19].

Hot radial pressing (HRP) was adopted as baseline joining technology [20,21]. Fig. 5 shows the HRP facility (with an internal view) employed for the mock-up production (a) and the graph of the process parameter history (b). Owing to the excellent wettability between copper and tungsten, the joining interface exhibited an excellent bonding quality even without diffusion. For the tungsten monoblock-type target design, the HRP technique has been well established and proven to be a highly reliable joining technology, also for series production. One drawback is the partial softening of the cooling pipe due to the thermal ageing (Ostwald ripening of precipitates) of CuCrZr alloy.

Two sorts of commercial grade tungsten materials were used for comparison, namely, ALMT (Japanese) and AT&M (Chinese). ITER material specifications (composition, density, hardness, grain size) were adopted for procurement [13]. Each test mock-up (consisting of four armor blocks) was manufactured with either ALMT tungsten or AT&M tungsten, respectively. Ultrasonic tests were conducted for all as-produced mock-ups for screening any defective features prior to HHF tests. Only sound and intact mock-ups were selected.

Fig. 6 shows typical microscopic images (left: optical after chemical etching, right: SEM backscatter electron) of an as-delivered AT&M tungsten block. Both images are displayed at the same magnification. It is noted that an optical micrograph unveils large-angle grain boundaries whereas a backscatter electron image reveals low-angle grain boundaries (or sub-grains). The optical micrograph shows aligned longish grains implying an underlying texture. On the contrary, the backscatter

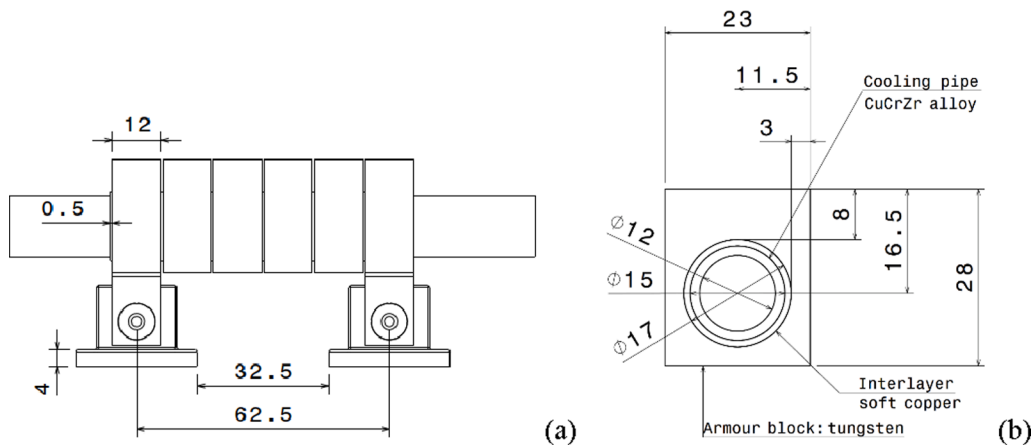


Fig. 4. Technical drawings of a target element segment (a: lateral view, b: cross section) [5].

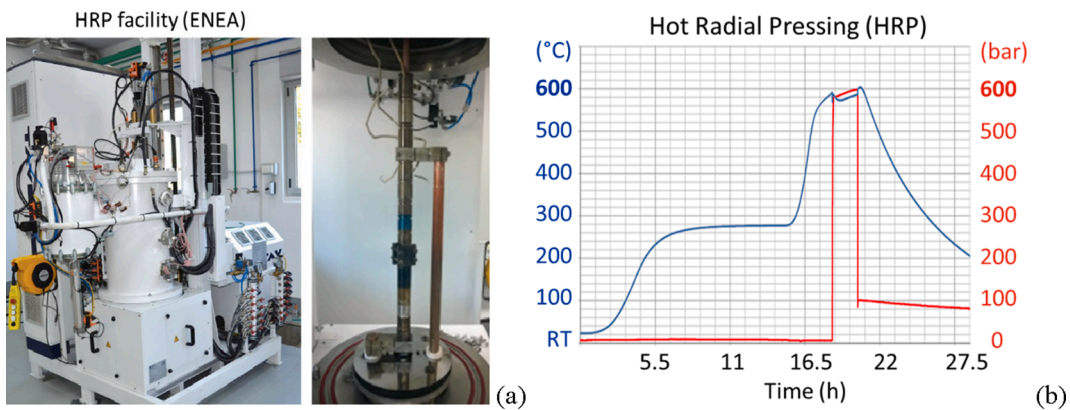


Fig. 5. HRP facility (with an internal view) employed for the mock-up production (a) and the graph of the process parameter history (b).

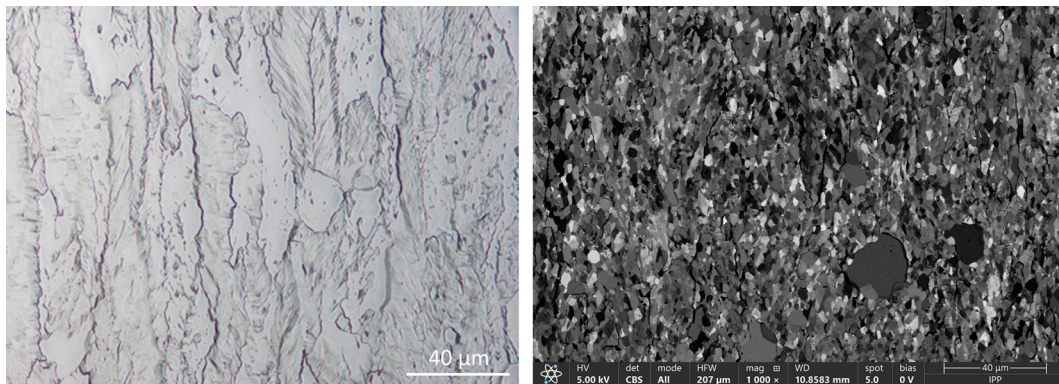


Fig. 6. Typical microscopic images (left: optical after chemical etching, right: SEM backscatter electron) of as-delivered AT&M tungsten.

electron image exhibits a much finer microstructure with an equiaxial shape.

Fig. 7 shows two sets of corresponding EBSD inverse pole figure crystal orientation maps produced for either AT&M tungsten or ALMT tungsten. Each set comprises three orientation maps all capturing the same microscopic region, but being displayed with three different misorientation threshold values (10° , 5° , 2°). Misorientation of 10° may be regarded as large-angle grain boundaries. AT&M tungsten exhibits a finer grain microstructure whereas ALMT tungsten shows a more apparent texture. However, the crystal orientation landscapes at the low-angle misorientation threshold (2°) seem to be comparable to each other. As the density of sub-grain boundaries may be supposed to be

proportional to dislocation density, the comparable sub-grain densities between the two tungsten grades indicate also comparable thermodynamic driving forces for recrystallization under the same heating condition.

Fig. 8 shows the standard pole figures of as-delivered AT&M tungsten, which manifest a strong initial texture formed by a hot rolling process.

Additionally, alternative design options have also been developed in WPDIV exploiting the advantages of innovative designs (thermal break), advanced materials (composite pipe) or novel joining techniques (graded interface) [14,22–27]. After a rigorous competitive evaluation process, the ITER-like design was selected as baseline HRF technology.

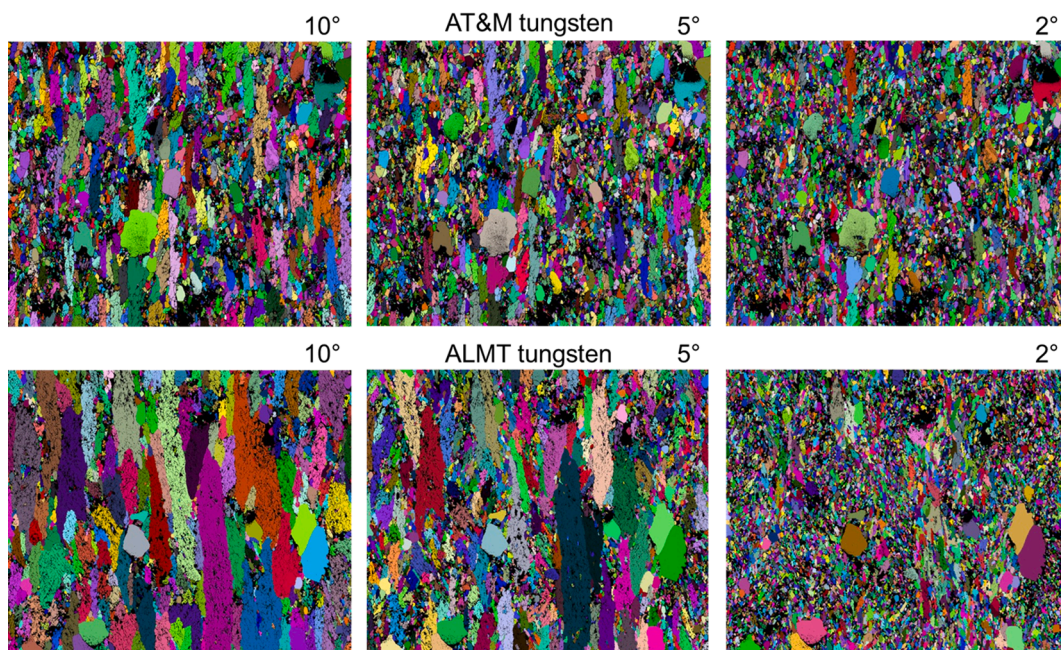


Fig. 7. EBSD inverse pole figure crystal orientation maps produced for AT&M tungsten or ALMT tungsten, respectively, where each set comprises three maps captured for the same microscopic region, but displayed with three different misorientation threshold values (10°, 5°, 2°).

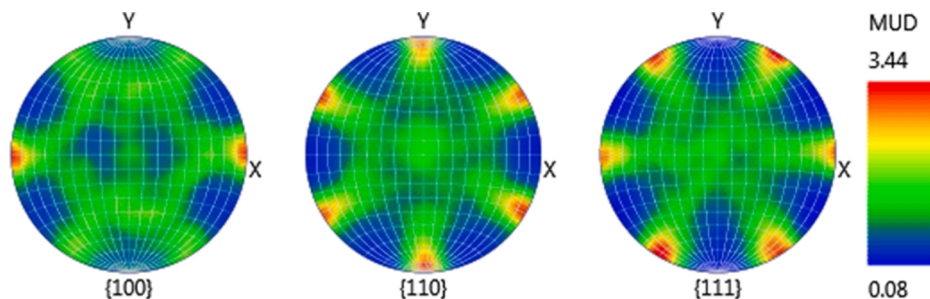


Fig. 8. Pole figures of as-delivered AT&M tungsten revealing a strong texture.

The impact of irradiation effects on potential structural failure risk was taken into consideration [10,28–30].

3. Thermal response of the target monoblock: Numerical prediction

A tungsten monoblock-type target element experiences a very steep temperature gradient under HHF loads. For instance, the calculated equilibrium temperature profiles building up in a single monoblock at

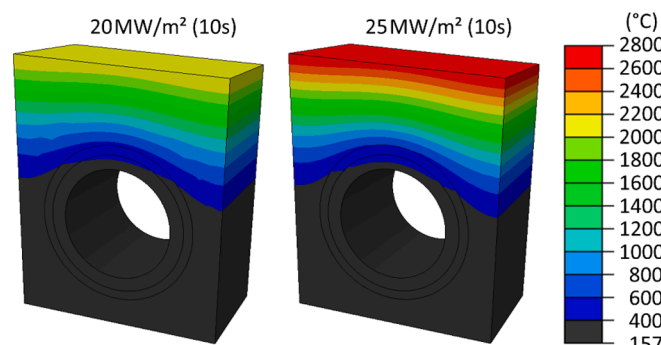


Fig. 9. Equilibrium temperature fields building up in a single monoblock at 20 MW/m² (left) and at 25 MW/m² (right).

20 MW/m² and 25 MW/m² respectively are plotted in Fig. 9. The simulation details are explained in Appendix A. In the tungsten armor (8 mm thick), the vertical temperature gradient reaches 200 °C/mm at 20 MW/m² and 275 °C/mm at 25 MW/m². At 20 MW/m², the temperatures in the upper half of the tungsten armor exceed the recrystallization temperature (1200–1300 °C). The maximum temperature at the front face reaches nearly 2200 °C at 20 MW/m² and 2800 °C at 25 MW/m². It is seen that only the lower half of the tungsten block remains below the DBTT (Ductile-to-Brittle Transition Temperature) of irradiated tungsten. The DBTT of commercial tungsten materials lies at around 560 °C [31]. Limited cracking could be potentially possible in this ‘cold’ region if tensile strength is drastically reduced by irradiation, probably due to transmutation. Furthermore, irradiation embrittlement would facilitate crack growth in stress concentration areas. On the other hand, irradiation hardening would give a beneficial effect in terms of yield strength. A dedicated recent study elucidated that the risk of cracking should be nonetheless subcritical even if the tungsten armor suffers from a considerable decrease of tensile strength and ductility [30]. Anyway, it seems highly unlikely that the ‘hot’ region of the armor would be affected by detrimental irradiation effects within the end-of-life damage dose and transmutation [10].

In Fig. 10, the steady state temperature field at 30 MW/m² is plotted. The temperature at the front surface reaches nearly the melting point of tungsten (=3422 °C). Thus, this heat load is the physical limit of thermal load for the given geometry. The temperature gradient increases to

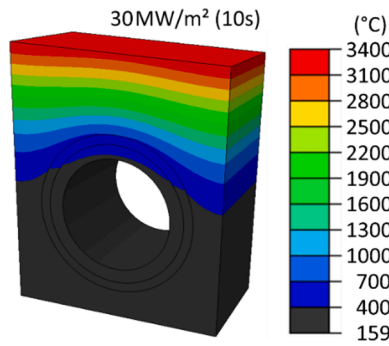


Fig. 10. Equilibrium temperature field at 30 MW/m².

338 °C/mm. The volume of the “cold” region (\leq DBTT) in the tungsten block remains almost unchanged.

4. HHF fatigue test: Objectives and methods

The purpose of this testing campaign was to evaluate the HHF performance of the tungsten monoblock-type target element under representative “slow” transient loading conditions (≥ 20 MW/m², ≥ 10 s). Slow transient events can take place in either normal (ramp-up/down) or off-normal (H-L transition) operation situations. In the testing, cyclic heat flux loads were applied to simulate repeated occurrence of transient heat pulses. Pulse duration time was set at 10 s, which was short enough to accumulate a large number of thermal cycles on one hand, yet still long enough to reach a dynamic thermal equilibrium within each heating cycle so that the entire mock-up being tested attained ultimate temperature profiles and thermal stresses. Two loading cases were applied: 20 MW/m² and 25 MW/m² (pulse: 10 s, cooling time: 30 s).

The HHF tests were conducted in high power beam facilities GLADIS (neutral hydrogen) and HADES (electron), respectively. Fig. 11 shows the view of both facilities with technical data. This comparative testing scheme using two different particle beams was motivated by the facts that the mode of beam irradiation (static vs scanning) and the beam/surface interaction features (penetration depth, reflection, chemical

effect) are different between the two facilities. In GLADIS, a Gaussian-type power density profile is produced by a static hydrogen beam whereas, in HADES, a time-averaged power density is produced by scanning of a quasi-focused electron beam [32,33]. The test results shall serve as empirical justification for the baseline HHF technology in the sense of “Design-by-Experiment” albeit in non-nuclear test conditions. Small-scale test mock-ups comprising four armor blocks (dimensions in Fig. 4) were used. The mock-ups were manufactured by means of the HRP process (580 °C, 600 bar) [19]. Ultrasonic inspection was carried out before and after the HHF tests for detection of potential defects and failure produced during either manufacturing or HHF testing [34]. Only intact mock-ups were used for the tests. Prior to the main tests, all mock-ups were subjected to preceding screening tests for checking the production quality in advance (Appendix B). Various in-situ or ex-situ diagnostic techniques were employed for detection of defects, for example, infrared (IR) thermography (in-situ, ex-situ), pyrometers, CCD camera, calorimetry (for power calibration), ultrasonic test (pre- and post-test), laser profilometry, and scanning electron microscopy (SEM) equipped with electron back-scatter diffraction (EBSD) [35–40].

5. Results: HHF fatigue tests in thermal equilibrium

The key topics of concern in this testing campaign are two folds:

1. Impact of cumulative thermal exposure on the microstructure of the armor materials
2. Impact of thermo-mechanical fatigue on the structural integrity of the joint

The underlying motivation of the present investigation was to specify the HHF performance limit of the current baseline technology in terms of the two topics above. It is noted that the test results would have been more or less different if the dimensions (armor thickness, block width, etc.) of the tungsten block were different. For the sake of completeness, selected data from the previous publications are referred here again.

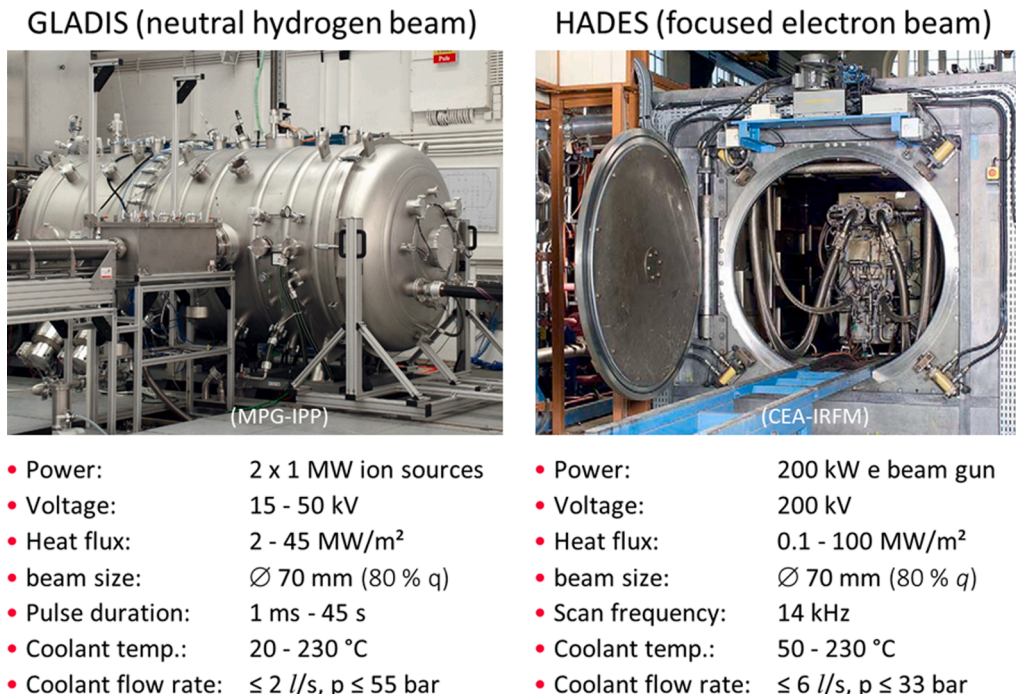


Fig. 11. High power beam facilities GLADIS and HADES employed for HHF testing.

5.1. Cyclic loading at 20 MW/m² (hydrogen beam)

Fig. 12 shows the front face of the tungsten blocks of two mock-ups after 500 heating cycles at 20 MW/m² tested at GLADIS (coolant: 130 °C, 40 bar, 16 m/s). The armor surface of the both mock-ups each with ALMT tungsten or AT&M tungsten respectively shows negligible or only modest deformation roughening. No crack was visible even on a microscopic scale. This finding was representative for all other 290 armor blocks tested at the same HHF load up to 500 cycles. The surface roughening was nearly saturated within 500 cycles and exhibited no further evolution at least up to 1000 heating cycles.

Fig. 13 shows the in-situ IR thermography images captured at the first and the 500th heating cycle during the HHF test. The false color temperature scale is indicative of surface temperature without an exact calibration. In principle, any relative change in surface temperature may indicate presence of a major defect (e.g. crack along the joining interfaces) which impedes heat conduction. In the present case, however, the apparent hot spots on the middle blocks are optical artefacts caused by changing emissivity due to the progressive surface roughening. The initial surface temperature measured by an one-color pyrometer (*T*-Kleiber) was slightly above 2000 °C.

In Fig. 14, the microstructure of the armor block (tungsten: ALMT) after the cyclic HHF test is presented. Shown is the metallographic section of one typical armor block (axial cut) with a superposed image of the EBSD map (inverse pole figure crystal orientation map) revealing the crystallographic landscape of the grain microstructure. In Fig. 15, the EBSD inverse pole figure map of Fig. 14 is shown again with a higher magnification in three consecutive depth regions. Each column consists of four sub-maps patched together.

No fracture or cracking is visible and the joining interfaces remained fully intact. The big grain locating in the front face layer (depth: 500–600 μm) indicates an irreversible change of microstructure resulting in such an abnormal grain growth. The EBSD map manifests that the big grain is fully monocrystalline [14]. The EBSD maps in Fig. 15 clearly reveal two distinct microstructural domains and their transition at the depth of around 4.5 mm from the front face. In the upper part above this transition depth, the tungsten armor is fully recrystallized up to the big single grain. The equi-axial grain shapes and the random crystal orientation distribution with large-angle grain boundaries indicate a mature recrystallization stage. On the contrary, the tungsten armor below this transition depth retains its initial fine-grained rolling texture. The temperature at the transition depth was roughly 1300 °C, which matched with the recrystallization temperature of tungsten. It is also seen that the copper interlayer (below 8 mm) has well-defined (no cell structure) coarse grains with large-angle grain boundaries. Annealing twins are also seen.

20MW/m², 500 cycles (coolant: 130°C)

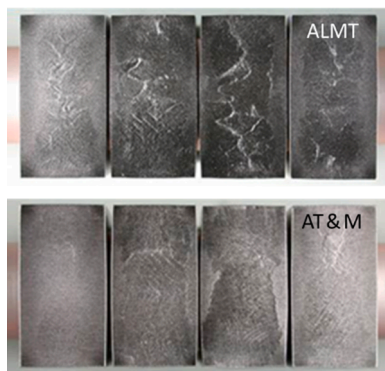


Fig. 12. Front face of the tungsten monoblocks of two test mock-ups (each with tungsten produced by ALMT and AT&M, respectively) after 500 pulses of cyclic loading at 20 MW/m² (coolant: 130 °C) [14].

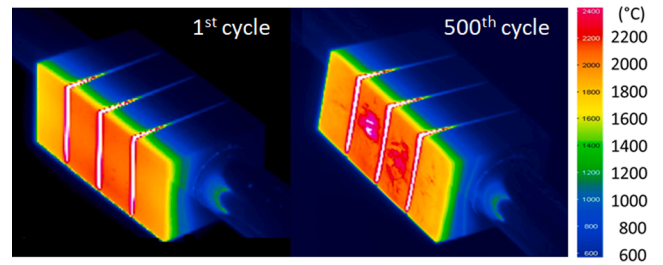


Fig. 13. In-situ infrared (IR) thermography images captured at the first and the 500th heating cycle during the HHF test at 20 MW/m² (coolant: 130 °C) [14].

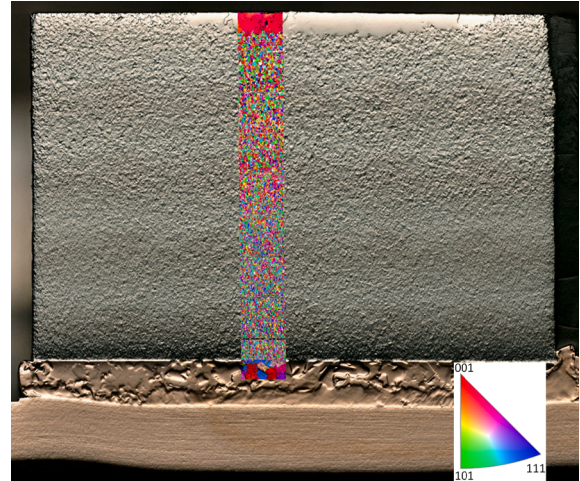


Fig. 14. Metallographic section of a typical armor block (axial cut, ALMT tungsten) after HHF test at 20 MW/m² up to 500 cycles. EBSD map is superposed along the thickness direction revealing the grains.

Fig. 16 shows the pole figures of the tungsten armor measured at eight depth positions (starting from the front surface) after 500 cycles of HHF loading at 20 MW/m². As already manifested in Fig. 15, the first two pole figures clearly indicate that the uppermost layer near the front face (depth range: 0–2 mm) is perfectly monocrystalline. On the other hand, the last two pole figures reveal that the lowest region near the interface to the copper interlayer (depth range: 7–8 mm) is characterized by a well-developed preferred orientation completely maintaining the initial rolling texture. It is recalled that the as-delivered tungsten showed the same pole figure feature (Fig. 8) as these ones. In the intermediate region (depth range: 2–6 mm), the orientation distribution becomes blurred implying nucleation of new grains with arbitrary crystal orientations. It is interesting to note that the visually discernible lower depth boundary of the recrystallized region in the inverse pole figure map (Fig. 15) does not seem to coincide with that of these pole figures (Fig. 16). Obviously, the grains in the depth range of 0–6 mm must have been fully recrystallized whereas the coarser equiaxial microstructure prevailing in the depth range of 2–4 mm should rather be attributed to subsequent grain growth of the recrystallized nuclei.

5.2. Extended cyclic loading at 20 MW/m² (electron beam)

HHF testing at 20 MW/m² was extended to 2000 heating cycles at HADES (coolant: 90 °C, 10 bar, 16 m/s). Due to a technical trouble, a reduced coolant temperature and pressure was applied. Fig. 17 shows the IR thermography images captured at the 1000th and the 2000th heating cycle. The front face of two heat-loaded tungsten blocks is also shown. In (b), the left block after 2000 heating cycles is shown again in a higher magnification. The mock-up remained fully intact as evidenced by the uniform temperature field in the thermography images. The

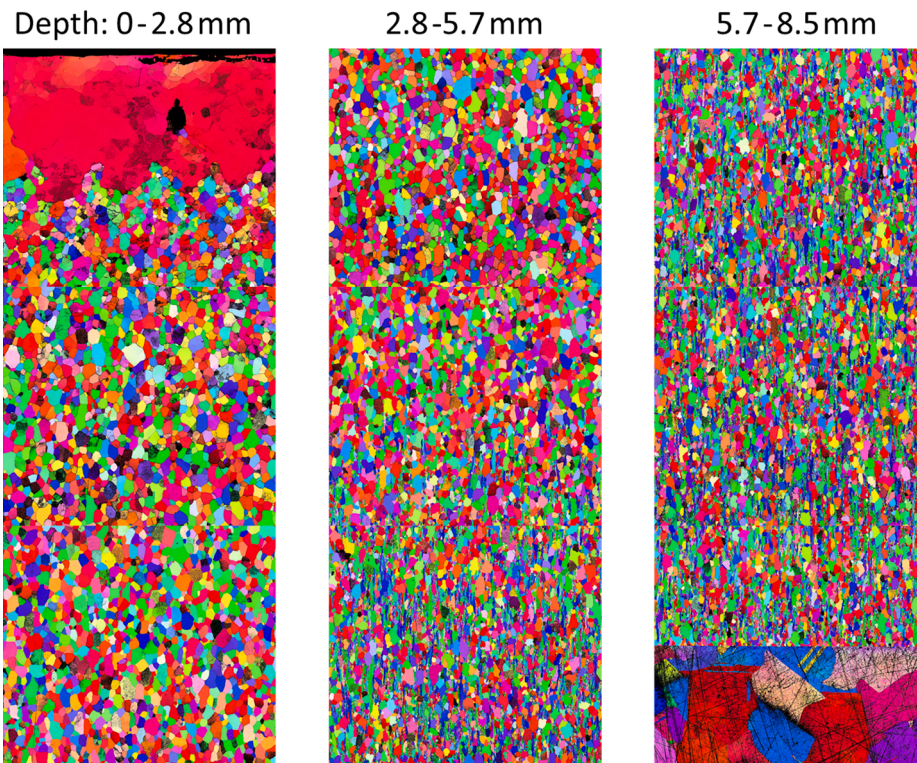


Fig. 15. EBSD scan map of Fig. 14 with a higher magnification for three consecutive depth regions.

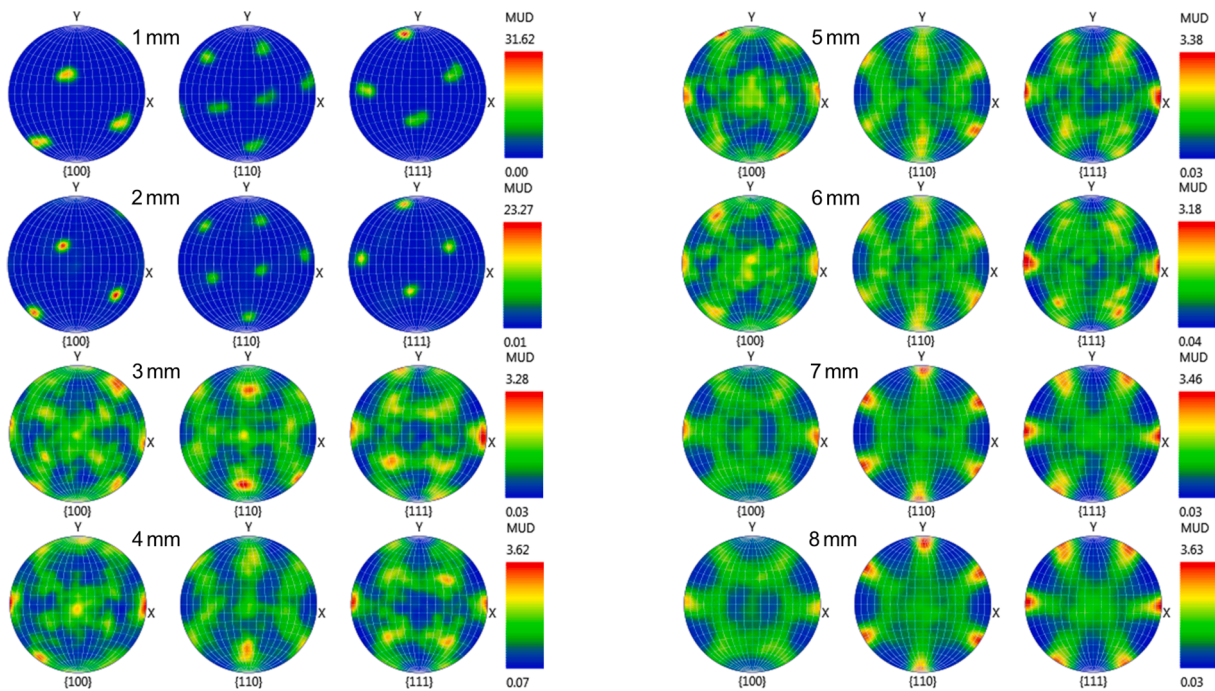


Fig. 16. Pole figures of the tungsten armor measured at eight depth positions covering the whole armor thickness after 500 cycles of HHF loading at 20 MW/m² (depth position starts from the front face).

armor front face exhibited only modest roughening. From around 1600 heating cycles on, a cluster of several small cracks began to form at one (right block) or two (left block) locations. Moreover, numerous fine micro-cracks formed on the surfaces of the tungsten blocks. However, these fine cracks did not grow further, but saturated in density and size.

A notable change was the bulging deformation of the blocks. The deformation progressed continuously in the course of the cumulative

heating cycles. Already after 1200 heating cycles, the neighboring blocks began to contact on the oval sides. After 1400 heating cycles, the lateral faces were mostly in contact. The bulging deformation was not discernible at least until 600 heating cycles.

It is recalled that the beam irradiation mode at HADES is different from that of GLADIS. The physical characteristics (e.g. penetration depth, reflectivity) of the carrier particles are also different. The impact

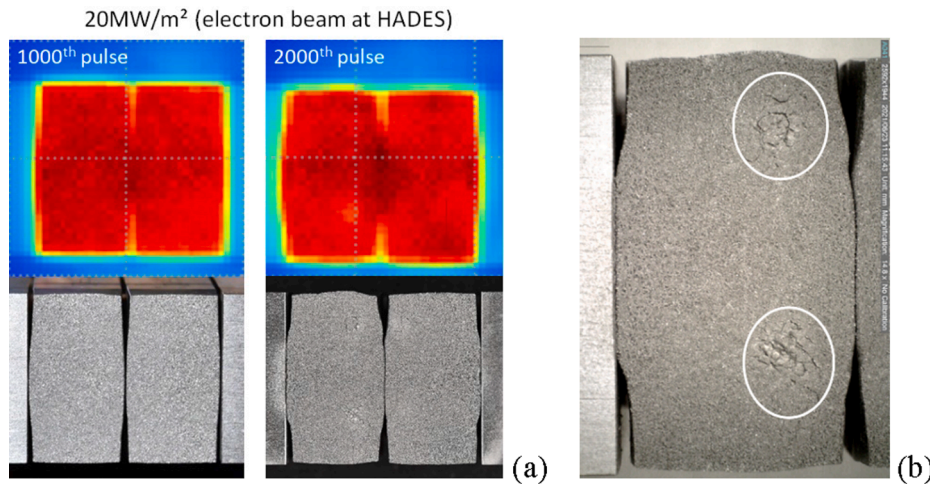


Fig. 17. (a) IR thermography images captured at the 1000th and the 2000th heating cycle at 20 MW/m² (coolant: 90 °C) and the corresponding front face of two heat-loaded tungsten blocks (AT&M). (b) The left block after 2000 heating cycles in a higher magnification.

of this difference on the test results still has not been fully identified yet. It is noted that the estimated heat flux density was not affected by reflectivity as the absorbed net power was calibrated by calorimetry.

5.3. Cyclic loading at 25 MW/m² (hydrogen beam)

Heat flux density was increased to 25 MW/m² as the final stage of the cyclic HHF fatigue test. 25 MW/m² was supposed to be the allowable upper limit of slow transient loads where pulse duration is long enough (several 10 s) to reach a thermal equilibrium in the entire monoblock. In the first test series, cold coolant (20 °C) was used to avoid critical coolant boiling which could lead to unexpected pipe rupture (and water leakage). In the subsequent test series, coolant temperature was carefully increased to 105 °C.

Fig. 18 shows the front face of the armor monoblocks (AT&M tungsten) after 100 and 500 cycles at 25 MW/m² (coolant: 20 °C) together with the IR thermography images. The mock-up remained apparently intact without any sign of structural failure. Note that the bright spots on the IR image at the 500th heating cycle are optical artefacts caused by the modified local emissivity due to the surface damage (roughness). The possibility that the bright spots could stem from a real temperature heterogeneity is deemed unlikely considering the rather high thermal conductivity and their tiny extension (heat conduction range). The armor surface exhibits progressive roughening

damage produced by inelastic deformation. At least until 100 cycles, the surface shows only modest roughening. After 500 cycles, the surface looks severely damaged as characterized by the pronounced roughening. The bulging deformation led to a diffusion bonding of the adjacent blocks. The deformation damage was clearly visible on the lateral faces of the mock-up up to 2–3 mm depth from the front face. The surface temperature measured by the one-color pyrometer (*T*-Kleiber) was slightly above 2500 °C.

In order to quantify the front face roughening damage, the surface topography was measured by means of laser profilometry. For comparison, the same HHF test was repeated with hot water cooling (105 °C) using a new mock-up (ALMT tungsten) to see the impact of higher coolant temperature. Fig. 19 shows the profilometry scan images together with the front face photographs after 500 cycles at 25 MW/m². Qualitatively, the deformation feature and roughening pattern look mostly similar between the two cases. The roughening pattern exhibits a symmetric topography characterized by two parallel hills forming at both outer side edges of the blocks. The upheaval progressed proportionally to the number of heating cycles. The height of the edge hills ranged between 600 and 650 μm. In the middle region, the relative roughness ranged between 200 and 400 μm. Such a pronounced roughening height may cause leading edge overheating by grazing SOL particles.

Fig. 20 shows the ultrasonic echo images scanned on the joining interfaces along the perimeter of the cooling pipe before and after 500 heating cycles at 25 MW/m² (coolant: 20 °C). Appearance of hot spots indicates presence of defects. The reflected echo intensity remained uniform at both interfaces also after the HHF test except for the sporadic minor defects locating near the outer edge of the interlayer/cooling pipe interface in the 4th block. Obviously, these small defects were produced during the joining process. Remarkably, these defects did not extend at all during the test. The ultrasonic scan images manifest overall intact joining interfaces at least up to 500 heating cycles at 25 MW/m².

Fig. 21 shows the metallographic cut sections of two armor blocks (ALMT tungsten) of another mock-up tested at 25 MW/m² (coolant: 20 °C) up to 100 heating cycles. The extent of abnormal grain growth is clearly visible as revealed by the optical contrast of large grains whereas the depth of the far reaching heat-affected zone is not discernible on this micrograph. The bond interfaces of the joint remained fully intact. On the other hand, the tungsten armor near the front face exhibits one or two thin vertical cracks, which initiated at the surface and grew up to 6 mm. Moreover, a few pores were created in the uppermost heat-affected zone. It is noted that the tungsten blocks were sound and free of defects in the as-delivered state before HHF tests. Apparently, the cracks and

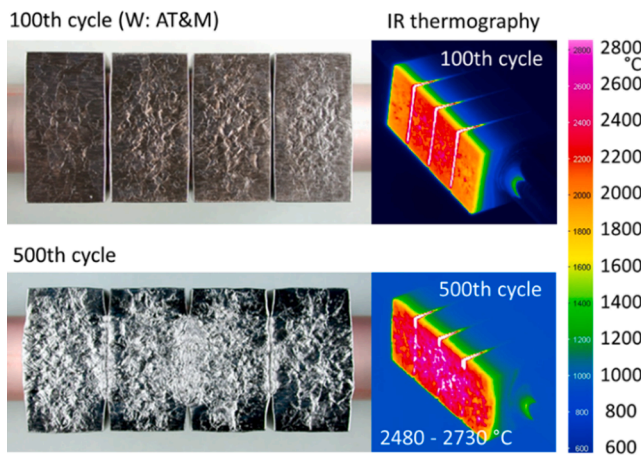


Fig. 18. Front surface of the armor monoblocks (AT&M tungsten) after 100 and 500 heating cycles at 25 MW/m² (coolant: 20 °C) and corresponding in-situ IR thermography images.

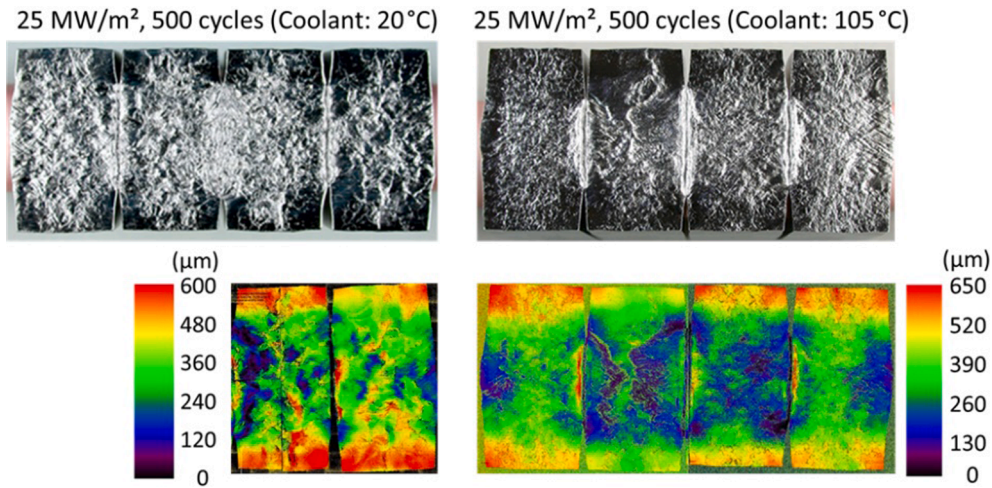


Fig. 19. Photographs and laser profilometry scan images of the armor front surface revealing roughening topography after 500 heating cycles at 25 MW/m² (coolant: 20 °C and 105 °C, respectively).

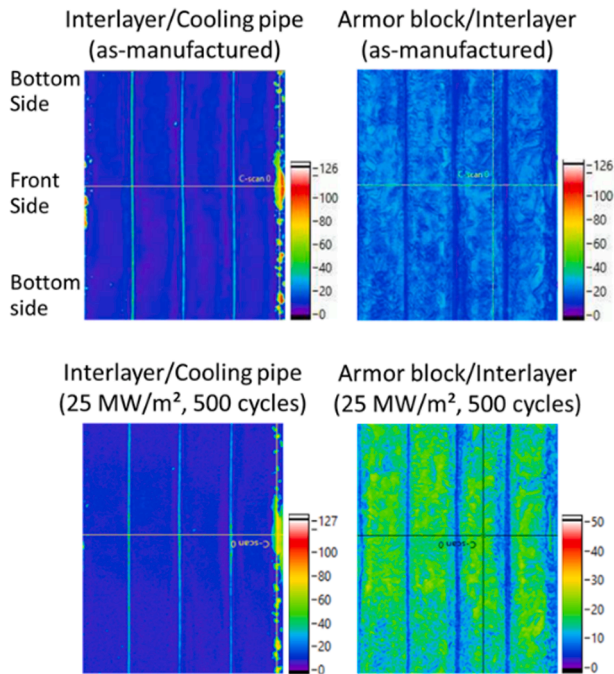


Fig. 20. Ultrasonic reflectometry images scanned on two joining interfaces along the perimeter of the cooling pipe before and after the HHF test at 25 MW/m² (coolant: 20 °C) up to 500 heating cycles.

pores did not appreciably affect heat removal capacity or structural integrity on a macroscopic scale.

Fig. 22 shows two metallographic cut sections (left: cross, right: axial) of the mock-up (AT&M tungsten) tested at 25 MW/m² (coolant: 20 °C) up to 500 heating cycles. The micrographs confirm that both bond interfaces are fully intact as indicated by the IR thermography and the ultrasonic inspection. The armor front face exhibits more progressed roughening deformation compared to the case of 100 heating cycles (cf. Fig. 21). A single fine crack is visible that was initiated at the middle of the front surface and grew down to about 6 mm depth. Comparing to Fig. 21, it is concluded that this crack must have been created in the early stage of the HHF test and ceased to grow very probably within 100 heating cycles. As the crack is very thin and stable, it seems harmless giving no actual impact on heat conduction as well as structural integrity. Another defect type is microscopic void either in form of a cluster or

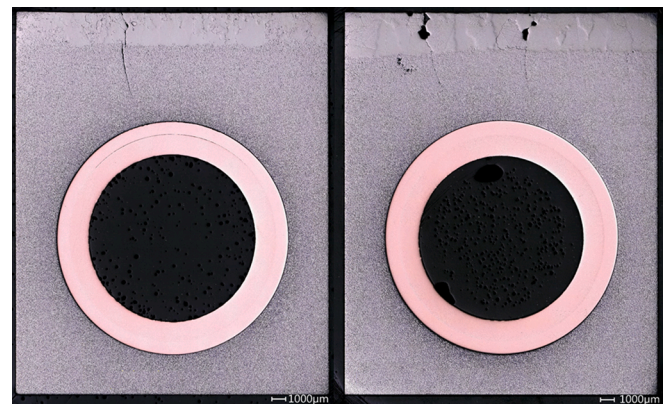


Fig. 21. Metallographic cross cut sections of two armor blocks (ALMT tungsten) of a mock-up tested at 25 MW/m² (coolant: 20 °C) up to 100 heating cycles.

isolated one (indicated by white arrows). Also these voids seem to be innocuous as there is no sign of failure initiating at these voids. On the axial cut section, the optical contrast reveals three distinguishable microstructural layers.

Fig. 23 shows the metallographic sections (axial cut) of two armor blocks (AT&M tungsten) each tested at 25 MW/m² (coolant: 20 °C) up to 100 (left) or 500 (right) heating cycles respectively. A partial EBSD map is superposed on each micrograph. Both EBSD maps exhibit a similar microstructural landscape where three clearly distinguishable domains are found. The distinctive microstructural feature of each domain starting from the front face is 1) extraordinary big grains (abnormal grain growth), 2) equi-axial coarse grains (recrystallization) and 3) textured fine grains (hot rolling), respectively. The three domains coincide well with the optical contrast boundaries of the corresponding micrograph. Each layer is about 2–3 mm thick. It is noteworthy that the microstructural features have already been coined within first 100 heating cycles and remained mostly stable in the subsequent heating cycles. The lower front of the recrystallized domain progressed by 1 mm downward between the 100th and 500th cycle.

The number of heating cycles was further increased to 1000 (coolant: 105 °C). The resulting deformation damage of the armor front face is shown in Fig. 24. For comparison, the surface after 500 heating cycles is also shown. The deformation roughening continued to develop resulting in a markedly aggravated damage state. The laser profilometry map after 1000 heating cycles clearly reveals a symmetric deformation

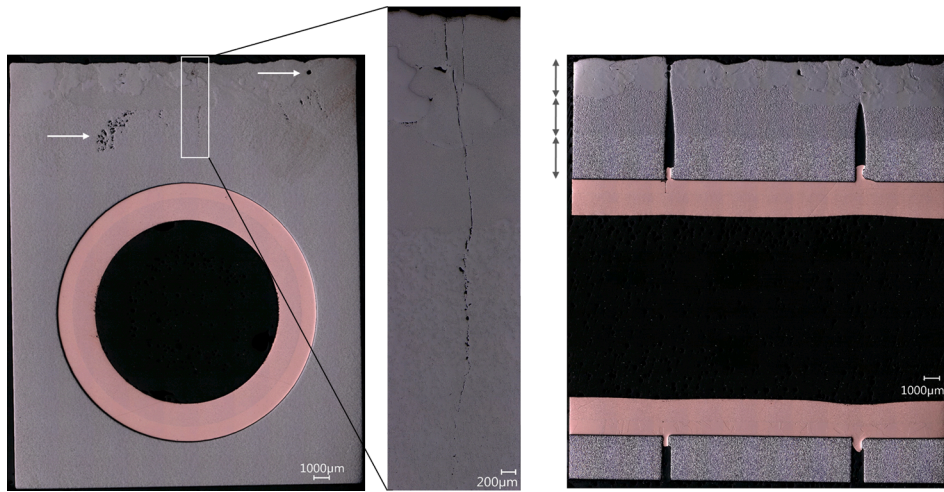


Fig. 22. Metallographic cut section of two armor blocks (AT&M tungsten) of the mock-up tested at 25 MW/m² (coolant: 20 °C) up to 500 heating cycles.

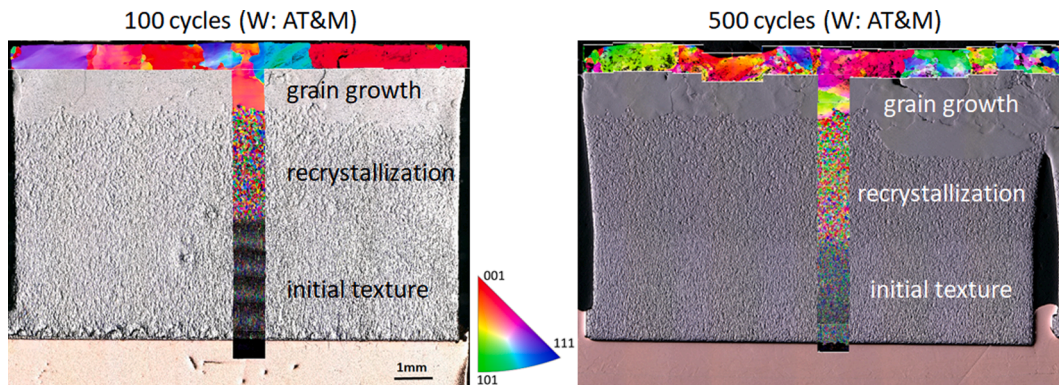


Fig. 23. Metallographic sections (axial cut) of two different armor blocks (AT&M tungsten) tested at 25 MW/m² (coolant: 20 °C) up to 100 (left) and 500 (right) heating cycles, respectively.

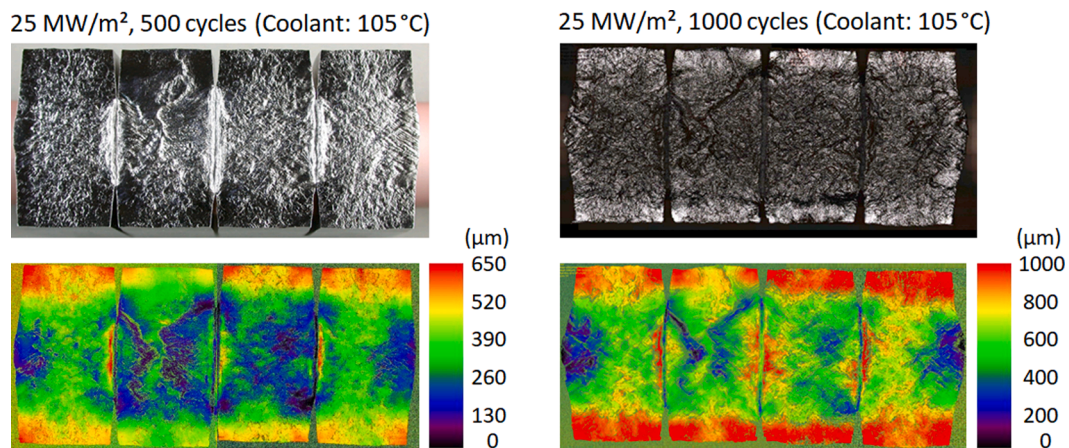


Fig. 24. Photographs and laser profilometry scan images of the armor front surface revealing roughening topography (ALMT tungsten) after 500 and 1000 heating cycles at 25 MW/m² (coolant: 105 °C).

topology characterized by the well-developed parallel hills locating at the outer edges of all blocks. The maximum height amounts to about 1 mm, which is a considerable offset from the initial front face level. The average difference in roughening height in the middle region increased significantly as well. The risk of the leading edge overheating becomes more serious. A dedicated study (experimental and computational) to assess the risk seems to be necessary. The deformation mechanism of the

symmetric hill formation has not been clarified yet. Creep straining by viscous flow is deemed a major contributor to the front face deformation and damage [41].

5.4. Cyclic loading at 25 MW/m² (electron beam)

Cyclic HHF test at 25 MW/m² was repeated using electron beam at

HADES (coolant: 50 °C). Fig. 25 shows the armor front surface after 300 and 500 heating cycles and the corresponding IR thermography images. The IR images show no emerging or evolving hot spots indicating intact integrity. The minor change in color shading is an optical artefact caused by the modified emissivity. The armor front face looks significantly less damaged exhibiting only modest roughening compared to the previous hydrogen beam irradiation case. A thin surface crack was formed on the left armor block. The crack was initiated already at around 100 heating cycles and remained stable thereafter. Generally, tungsten armor loaded by electron beam tended to show a benign surface damage compared to neutral hydrogen beam. However, the physical reason for this remains open.

5.5. Impact of melting: Cyclic loading at 20 MW/m² after solidification (hydrogen beam)

In a fusion operation of a DEMO reactor, it is assumed that off-normal slow transients or even disruption would not be perfectly suppressed. In such accidental circumstances, partial melting of the tungsten armor will be likely to occur due to the excessive heat deposition. If the molten armor layer is not fully splashed away, but solidifies again, the armor will undergo a resetting of the microstructure. It is worthy of investigating the HHF performance of the resolidified armor to examine the feasibility of the reuse option. To this end, we deliberately applied a controlled overload at 35 MW/m² (pulse: 5.3 s) in order to produce a molten layer on the front face (~2 mm depth). After solidification, a HHF fatigue test was conducted at 20 MW/m² (coolant: 130 °C) up to 1000 heating cycles.

Fig. 26 shows the front face of two armor blocks in the middle (AT&M tungsten) solidified after melting and the damaged surface of the same blocks after the HHF test. The armor exhibits no notable difference in roughening damage behavior between the solidified blocks (in the middle) and the other two blocks (at the sides). The relative height of roughening after the HHF loading reaches around 600 μm in the middle region (Fig. 27). The hill (bottom side) and the crater (top side) are artefacts produced by gravity acting on the liquid tungsten layer upon melting. Only a minor increase of height is seen at the hill after the cyclic HHF loading. The mock-up remained fully intact during the HHF test showing no temperature increase as manifested by the IR thermography and the optical images in Fig. 28.

Fig. 29 shows the metallographic section of the mock-up (upper part) with the solidified armor blocks after 1000 heating cycles at 20 MW/m². The front face region exhibits more severe inelastic deformation roughening compared to Fig. 12. No major crack is found. Several small pores exist either in isolation or in a cluster. However, these pores seem to be benign as no failure was initiated by any of them. A local delamination of the interlayer/pipe interface near the gap is also observed.

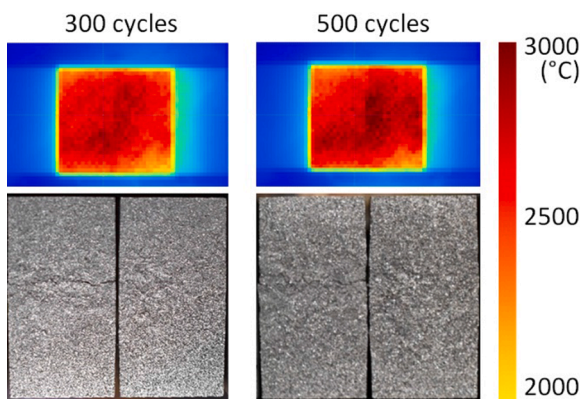
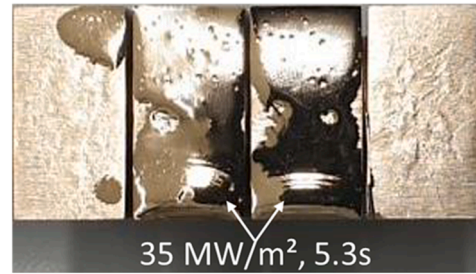


Fig. 25. Front surface of the armor monoblocks (AT&M tungsten) after 300 and 500 heating cycles at 25 MW/m² (coolant: 50 °C) and corresponding in-situ IR thermography images captured during electron beam irradiation test.

After melting of two middle armor surface

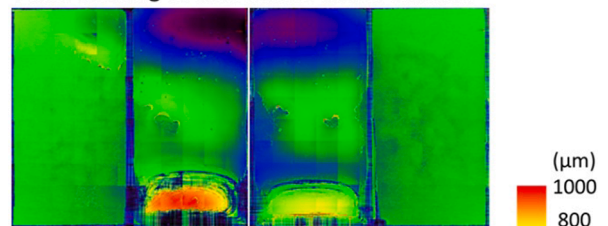


After HHF loading (20MW/m², 1000 cycles)



Fig. 26. Photographs of the front surface of two armor blocks (in the middle) solidified after melting at 35 MW/m² (pulse: 5.3 s) and the damaged surface of the same blocks after 1000 heating cycles at 20 MW/m² (coolant: 130 °C).

After melting of two middle armor surface



After HHF loading (20MW/m², 1000 cycles)

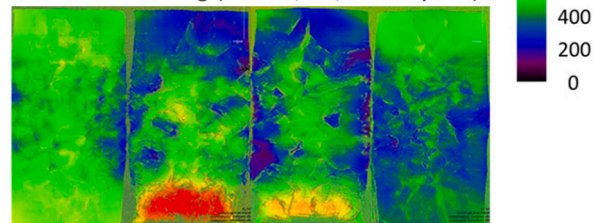


Fig. 27. Laser profilometry scan images of the as-solidified armor blocks after melting (two blocks in the middle) and the same armor blocks after 1000 heating cycles at 20 MW/m² (coolant: 130 °C).

The cause of this delamination is attributed to cumulative plastic damage due to local fatigue and ratchetting [10,42–44].

Fig. 30 shows the EBSD scan map of the metallographic section given in Fig. 29 (middle block). The microstructural landscape is apparently analogous to the loading case at 25 MW/m² rather than the case at 20 MW/m² in the sense that the range of the big grains (~2 mm) is comparable to that of Fig. 23 while it is wider than the monocrystalline layer in Fig. 14. However, it should be noted that the big grains in Fig. 30 were primarily formed by solidification of the molten layer, not necessarily by abnormal grain growth alone. The individual big grains seem to contain sub-grains or cell structures as revealed by the low-angle misorientations. Such dislocation-rich sub-grains are thought to be a consequence of plastic straining facilitated by softening of the solidified grains.

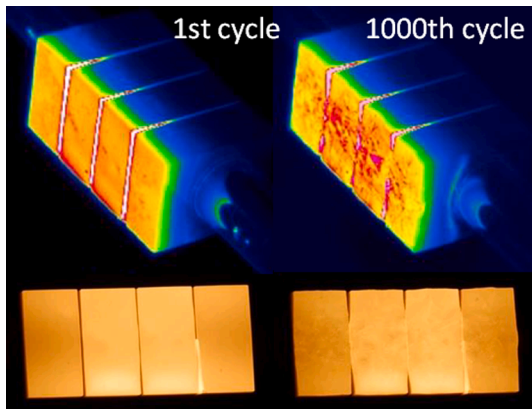


Fig. 28. IR thermography images and CCD camera images of the solidified armor blocks (two blocks in the middle) captured at the 1st and the 1000th heating cycle at 20 MW/m² (coolant: 130 °C).

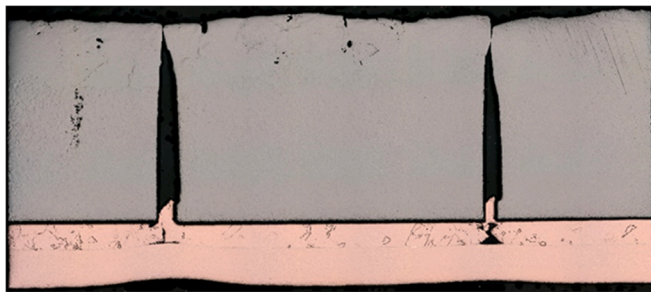


Fig. 29. Metallographic section (axial cut) of the mock-up (upper part) with the solidified armor blocks after 1000 heating cycles at 20 MW/m² (coolant: 130 °C).

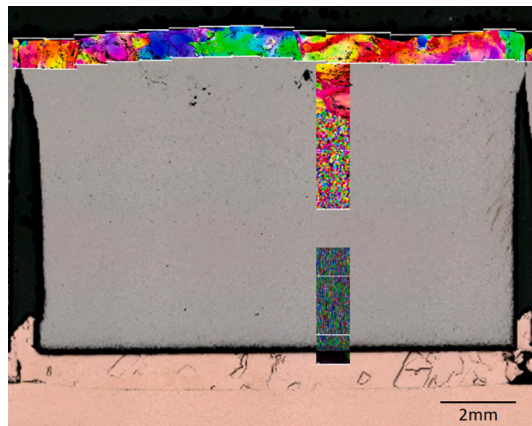


Fig. 30. EBSD scan map superposed on the metallographic section (Fig. 29) of the mock-up with the solidified armor blocks after 1000 heating cycles at 20 MW/m² (coolant: 130 °C).

6. Results: HHF fatigue tests under short transients

In case a slow transient takes place imposing unacceptably heavy thermal load on the target strike point, a mitigation measure must be immediately activated before the affected target is severely damaged and becomes inoperable. One of the potentially applicable measures is magnetic sweeping of the strike point by means of a dedicated in-vessel coil [45,46]. In EU-DEMO, the maximum heat flux density upon an unmitigated slow transient is predicted to amount to 70 MW/m². If the strike point is swept over the poloidal span of 20 cm with 1 Hz

frequency, the time-averaged heat flux density could be reduced down to roughly 40 MW/m² with a short pulse duration (0.3–0.4 s) at each position in the sweeping range. Under such a short transient load, the heat pulse will mostly affect the near-surface layer of the armor blocks while the distant cooling pipe will not experience the acute impact of the heat wave.

6.1. Cyclic shocks at 40 MW/m², 0.4 s (hydrogen beam)

In order to simulate the short transient sweeping case, a tailored HHF test was conducted where a cyclic heat flux load of 40 MW/m² with the pulse duration of 0.4 s and the heating frequency of 0.63 Hz was applied up to 5000 cycles. Two mock-ups each with ALMT or AT&M tungsten respectively were tested. Fig. 31 shows the measured (pyrometer) and the FEM-computed armor surface temperature history in the first 10 heating cycles. The front surface temperature reaches roughly 1900 °C.

Fig. 32 shows the front face of the tungsten blocks after 5000 heating cycles and the IR thermography images captured at 500th and 5000th heating cycle. The armor surface exhibits only modest or negligible roughening. No crack or damage is visible. The constant surface temperature indicates fully intact joints.

Fig. 33 shows the laser profilometry scan images of the armor front face at five selected stages of heating cycles. The armor blocks exhibit a peculiar deformation topography where two symmetric hills formed. The height of the hills increased nearly in proportion to the cumulative number of heating cycles. The AT&M tungsten blocks showed a higher peak height (350 μm) than the ALMT tungsten blocks (250 μm). The deformation topography pattern under the short transient loading is notably different from that of the slow transient loading (cf. Fig. 24). At least up to 5000 heating cycles, the elevation of the hills has not yet reached saturation.

Fig. 34 shows the metallographic section of the armor blocks (AT&M tungsten) with the superposed EBSD scan map after 5000 cycles. The microstructural transition between the lower domain with fine-grained texture and the upper domain with equi-axial recrystallized grains are clearly seen. In contrast to the slow transient cases (pulse: 10 s), where the heat-affected armor underwent abnormal grain growth as well as recrystallization (cf. Figs. 14, 23), under the short transient loads, only recrystallization took place in the whole heat-affected zone. This difference is attributed to the much shorter cumulative heat exposure time in the short transient loading case (~1100 s for ≥ 1500 °C, ~250 s for ≥ 1800 °C) compared to the slow transient loads (~8500 s for ≥ 1500 °C, ~7000 s for ≥ 1800 °C). The negligible roughening is attributed to the absence of big soft grains which otherwise would undergo heavy inelastic deformation producing pronounced roughening and damage of the front surface.

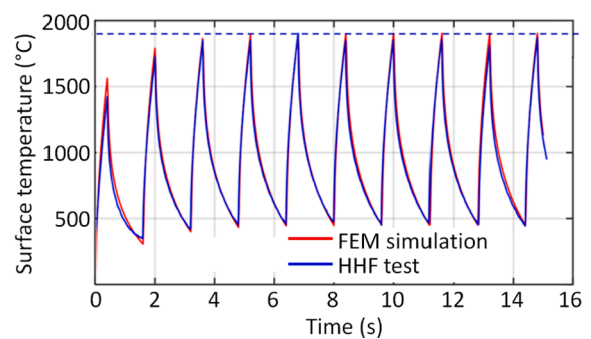


Fig. 31. Measured (pyrometer) and the FEM-computed armor surface temperature history in the first 10 heating cycles of the HHF test at 40 MW/m² (pulse duration: 0.4 s, frequency: 0.63 Hz).

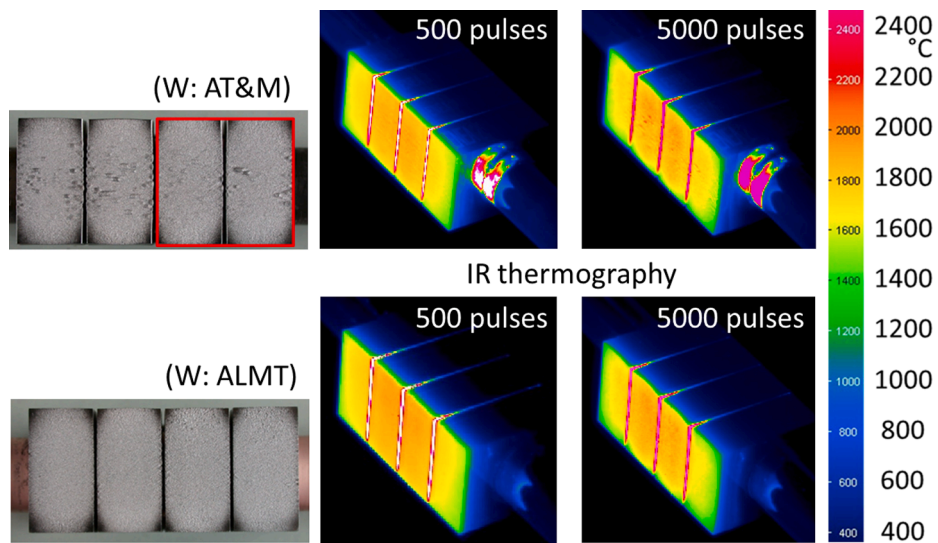


Fig. 32. Post-test photographs and in-situ IR thermography images of the armor front surface (AT&M and ALMT tungsten, respectively) at 500th and 5000th heating cycle of 40 MW/m² (pulse: 0.4 s, frequency: 0.63 Hz, coolant: 130 °C).

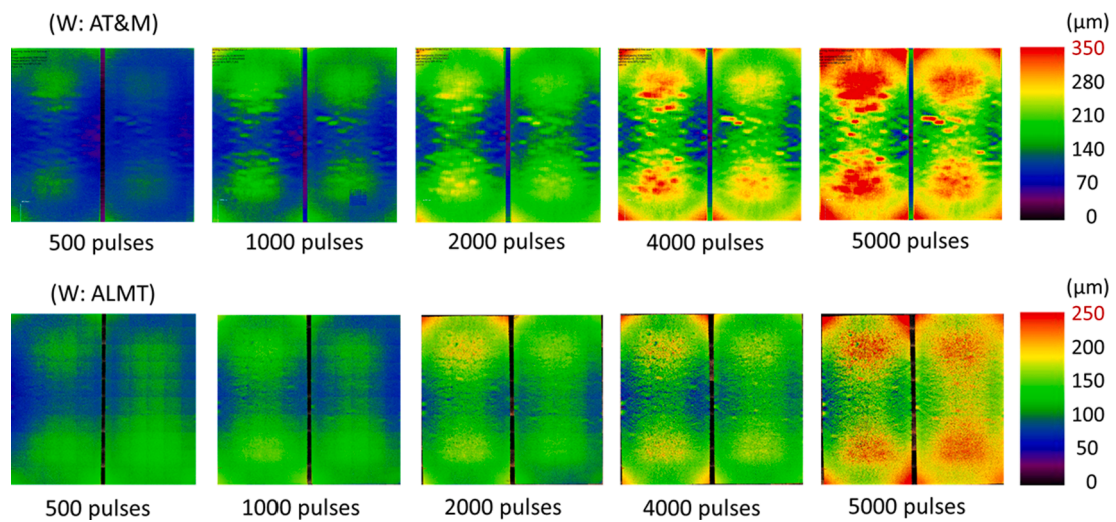


Fig. 33. Laser profilometry scan images of the armor front surface at five selected heating cycles (heat flux: 40 MW/m², pulse: 0.4 s, frequency: 0.63 Hz, coolant: 130 °C).

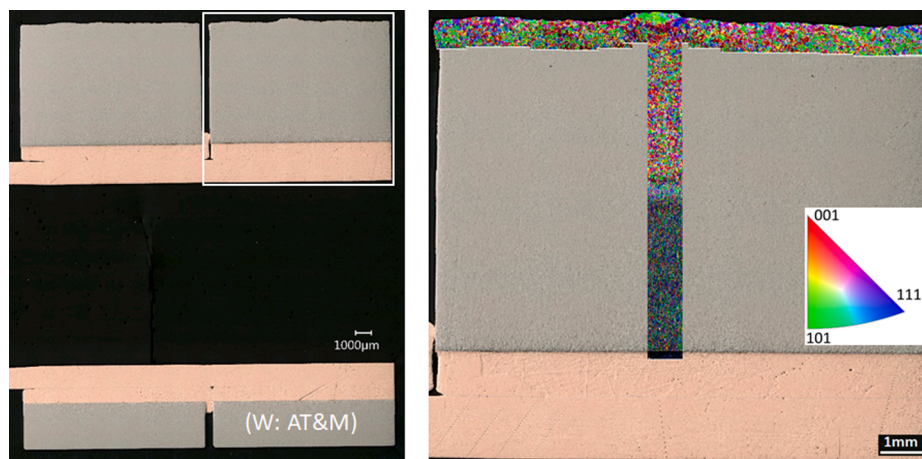


Fig. 34. Metallographic section (axial cut) of the armor blocks (AT&M tungsten) with the EBSD scan map (right) after 5000 short transient heating cycles at 40 MW/m² (pulse: 0.4 s, frequency: 0.63 Hz, coolant: 130 °C).

7. Results: Ultimate HHF limit load

7.1. 31/32 MW/m², 10 s

Several mock-ups were loaded at 32 MW/m² (cold coolant, 5 cycles, hydrogen beam). This heat flux density is regarded as the maximum allowable thermal load because the maximum armor temperature is calculated to approach the physical limit, namely, the melting point. Unfortunately, a direct optical measurement was not possible because the installed pyrometers were not capable of detecting such high temperature. The mock-ups remained fully intact and the armor showed only slight surface roughening (Fig. 35). Under electron beam irradiation (coolant: 50 °C), initial melting began to occur at 31 MW/m² as indicated by local temperature decrease on the IR thermography image (dotted circles) in Fig. 36.

7.2. 37 MW/m², 10 s (electron beam)

The potential failure scenarios of the target that would possibly occur under an excessive thermal load are 1) massive melting of the armor, 2) critical fracture of the armor or the interfaces due to thermal stress or fatigue, 3) rupture of the cooling pipe due to overheating by coolant (film) boiling. It is a valid question which of these scenarios would occur first. To figure out this, we applied deliberately overloads up to 37 MW/m². This final heat load is beyond the critical heat flux density of armor melting (31–32 MW/m²) as well as the critical heat flux density of coolant nucleate boiling (33 MW/m² for the present applied cooling condition: 50 °C, 10 bar, 16 m/s). The heat flux was increased stepwise. The armor began to melt massively at about 33–34 MW/m² (Fig. 37). However, the joining interfaces and the cooling pipe remained fully intact. This result manifests the sufficient mechanical resilience against excessive HHF limit loads even beyond the critical heat flux limits (armor melting or coolant boiling) as long as the duration of a transient overloading is limited to about 10 s.

8. Summary and conclusions

Slow thermal transients foreseen during each plasma ramp-up or accidental reattachment pose a critical engineering issue for the DEMO divertor targets since the expected overloads (≥ 20 MW/m²) far exceed the design load prescribed for the normal operation (≤ 10 MW/m²). The baseline HHF technology of the EU-DEMO based on the ITER-like tungsten monoblock concept must be qualified also for the overload regime before it is validated as eligible technology for verification of full-scale prototype production.

For evaluation of the performance of the baseline HHF technology in the overload regime, we conducted an extensive testing campaign using small-scale test mock-ups of the tungsten monoblock target for two slow (10 s) transient overloads at 20 MW/m² and 25 MW/m², and for a short (0.4 s) transient overload at 40 MW/m². In-situ IR thermography, ultrasonic inspection and electron microscopy delivered valuable information and direct insight on the structural integrity of the joints and the microstructural impact on the armor materials. The major findings are

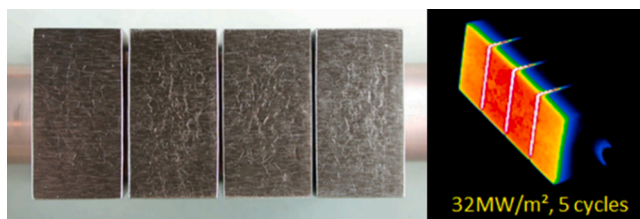


Fig. 35. Front face of the monoblocks (AT&M tungsten) after 5 heating cycles at 32 MW/m² (coolant: 20 °C) and corresponding in-situ IR thermography image.

31 MW/m²

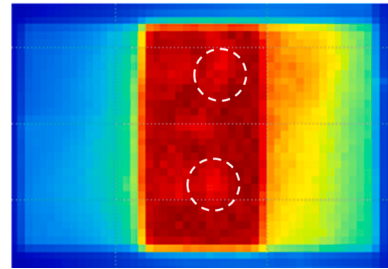


Fig. 36. In-situ IR thermography image at 31 MW/m² under electron beam irradiation (coolant: 50 °C).

as follows.

1. 20 MW/m² (pulse: 10 s, coolant: 130 °C): all tested mock-ups remained fully intact at least up to 1000 heating cycles. One selected mock-up survived 2000 cycles without any failure. The tungsten armor underwent full recrystallization in the depth range of 5 mm from the front surface and abnormal grain growth in the depth range of 1–2 mm. The armor surface exhibited negligible roughening damage and dimensional change up to 500 cycles. After 2000 cycles, the blocks showed oval deformation, but little damage.
2. The tungsten armor solidified after controlled surface melting survived 1000 cycles at 20 MW/m² exhibiting a similar damage and roughening feature as the armor which had not been molten.
3. 25 MW/m² (pulse: 10 s, coolant: 20 °C or 105 °C): Three mock-ups remained nearly intact at least up to 500 heating cycles. One selected mock-up survived 1000 cycles without failure. Only an innocuous fine crack was found which was initiated at the front surface and grew up to 6 mm depth. The tungsten armor underwent full recrystallization in the depth range of 6 mm and abnormal grain growth in the depth range of 2–3 mm. The microstructural changes of the armor were completed already before 100 heating cycles and remained nearly saturated in the following 400 heating cycles. The armor surface showed substantial inelastic deformation producing pronounced roughening and symmetric hills with the height of 650 μm after 500 cycles and 1000 μm after 1000 cycles.
4. The overall structural integrity at 20 MW/m² and 25 MW/m² was verified for both neutral hydrogen beam and electron beam irradiation. The armor blocks of ALMT tungsten and of AT&M tungsten showed comparable HHF fatigue behaviors and very similar microstructural changes at both HHF load cases applied.
5. 40 MW/m² (pulse: 0.4 s, frequency: 0.63 Hz, coolant: 130 °C): both tested mock-ups remained fully intact without any considerable deformation damage at least up to 5000 cycles. On the armor surface, two symmetric hills formed and grew proportionally to the number of heating cycles. The height of the hills reached 250 μm (ALMT) or 350 μm (AT&M) after 5000 cycles. Only full recrystallization occurred in the upper half of the armor without abnormal grain growth.
6. Selected mock-ups (20 monoblocks) were loaded up to 32 MW/m² (cold coolant, 5 cycles, hydrogen beam). The mock-ups remained fully intact showing only benign surface roughening.
7. Under increasing overloads massive melting of the armor occurred first at 33–34 MW/m² while the joining interfaces and the cooling pipe still remained fully intact up to 37 MW/m² although the critical heat flux density of coolant nucleate boiling (33 MW/m²) was far exceeded.

Based on these findings, following conclusions could be drawn:

1. The tungsten monoblock technology would be applicable for the long-pulse normal operation with the peak heat flux density of up to

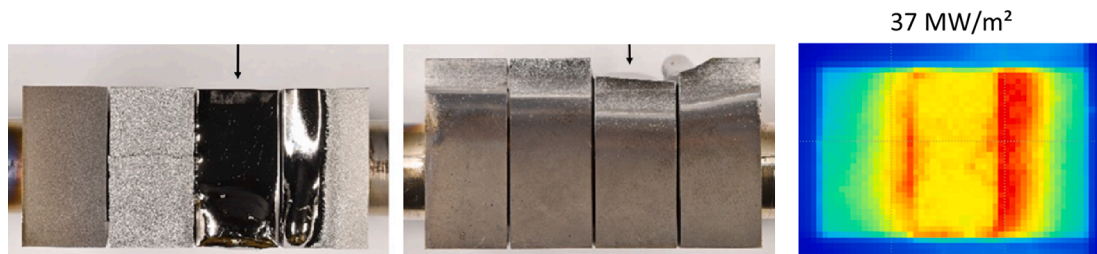


Fig. 37. Post-test photographs of the overloaded armor block (indicated by the arrow) after critical heat flux test at 37 MW/m^2 (left: front view, right: lateral view) and the in-situ IR thermography image.

- 20 MW/m^2 over the entire envisaged lifetime (≥ 7000 cycles). 20 MW/m^2 was also recommended as the maximum allowable heat load in terms of critical heat flux of coolant boiling by the ITER team [47]. This would mean that design heat load could be specified at 15 MW/m^2 with the safety margin of 5 MW/m^2 . The maximum heat load during each ramp-up/down (as a part of the normal operation phase) must be reduced to this design heat load level by aggressive radiative cooling (at least 85–90 %). The lifetime of the armor will be solely dictated by the transient events whereas normal operation (except ramp up/down) will have de facto no detrimental impact.
- This technology would probably withstand repeating slow transients (~ 10 s) up to 25 MW/m^2 for a limited number of pulses (at least 1000 times) without losing the structural integrity of the joint and without critical fracture of the armor. However, the substantial roughening damage of the armor front face poses a critical concern in terms of the leading edge issue. Therefore, strike point sweeping or aggressive radiative cooling (~ 90 %) is recommended to reduce the peak heat flux down to 20 MW/m^2 .
 - For shorter plasma transients (< 1 s), a higher heat flux density could be accommodated owing to the shorter cumulative heat exposure time. For instance, the acceptable number of loading cycles would reach at least 5000 pulses at 40 MW/m^2 if the pulse is short enough (≤ 0.4 s). This capacity supports the idea of strike point sweeping upon a reattachment event with 70 MW/m^2 .
 - The irreversible microstructural changes of the tungsten armor per se do not seem to have adverse impact on the thermal or mechanical performance of the targets. Under heat loads around or above 20 MW/m^2 , the initial metallurgical features (and the merits thereof) will surely go fully lost. Thus, if transient overloads have to be accepted as unavoidable operational events, any metallurgical efforts towards engineered tungsten armor would deliver little or only limited benefits (if any) for the given design concept.
 - The tungsten monoblocks would have resilience against sporadic overloads up to 30 MW/m^2 without any catastrophic structural failure. The acceptable number of such acute overloads is still unspecified.
 - Thermal stress states (including the residual stress) will probably be modified by the repeated thermal (over)loads due to creep and material softening affecting the fatigue behavior [10,41,48].
 - It should be noted that the results presented here were obtained from non-nuclear HHF tests. Effects of neutron irradiation need to be taken into account for a reliable technology maturity assessment. Both experimental (HHF testing of irradiated mock-ups in a hot cell) and computational (code-based failure risk assessment) studies will remain mandatory [49–52].
 - The present HHF test results suggest that the HRP-based tungsten monoblock technology would offer the most promising potential to meet the heat exhaust capacity required for the EU-DEMO divertor. The empirically verified HHF performance limit of the baseline target technology was significantly extended by this study compared to the previous HHF test results of the ITER target mock-ups [53].

CRediT authorship contribution statement

Jeong-Ha You: Conceptualization, Methodology, Supervision, Writing – original draft, Writing – review & editing, Project administration, Funding acquisition. **Henri Greuner:** Conceptualization, Methodology, Investigation. **Bernd Bösowirth:** Investigation. **Katja Hunger:** Investigation. **Selanna Roccella:** Methodology, Investigation. **Helen Roche:** Methodology, Investigation.

Declaration of Competing Interest

The authors declare the following financial interests/personal relationships which may be considered as potential competing interests: Jeong-Ha You reports financial support was provided by Euratom Research and Training Programme. Jeong-Ha You reports a relationship with Euratom Research and Training Programme that includes: funding grants and travel reimbursement. A member of the editorial board of the Journal “Nuclear Materials and Energy”.

Data availability

Data will be made available on request.

Acknowledgement

This work has been carried out within the framework of the EUROfusion Consortium, funded by the European Union via the Euratom Research and Training Programme (Grant Agreement No 101052200 - EUROfusion). Views and opinions expressed are however those of the authors only and do not necessarily reflect those of the European Union or the European Commission. Neither the European Union nor the European Commission can be held responsible for them.

Appendix A

Transient thermal analyses were made by means of finite element method (FEM) using a commercial FEM code ABAQUS. A half symmetry model meshed with quadratic solid elements was used exploiting the axial symmetry. A uniform heat flux density was assumed on the front surface of the armor for the pulse duration of 10 s using DFLUX. Heat transfer at the pipe/coolant interface was defined using FILM. Temperature-dependent heat transfer coefficients were calculated using the Sieder-Tate correlation with a swirl tape correction [29]. The assumed coolant temperature and pressure was 150 °C and 50 bar. Data of the ITER SDC-IC were used for the thermal material properties [51,52]. Stefan-Boltzmann type radiation was also taken into account.

Appendix B. Screening tests

All individual mock-ups were subject to a preceding screening test for the purpose of non-destructive quality control prior to the main HHF fatigue tests. It was supposed that those mock-ups which initially had seemingly intact joining interfaces (according to the ultrasonic

inspection) would experience fast fracture or growth of a fatigue crack at a weak joining interface (if any) already in the early stage of a cyclic HHF loading if the joining quality was not as good as it should be. These mock-ups were sorted out before the elaborate main tests to avoid any unexpectedly premature failure. The generic procedure of the screening tests were as follows:

1. Stepwise increase from 5 MW/m² to 25 MW/m² with 5 cycles at each load level (coolant: 20 °C).
2. Cyclic heating at 10 MW/m² up to 100 pulses (coolant: 20 °C).
3. Stepwise increase from 5 MW/m² to 20 MW/m² with 5 cycles at each load level (coolant: 130 °C).

References

- [1] M. Turnyanskiy, et al., A roadmap to the realization of fusion energy: mission for solution on heat-exhaust systems, *Fusion Eng. Des.* 96–97 (2015) 361–364.
- [2] N. Asakura, et al., Plasma exhaust and divertor studies in Japan and Europe Broader Approach DEMO Design Activity, *Fusion Eng. Des.* 136 (2018) 1214–1220.
- [3] N. Asakura, et al., Power exhaust concepts and divertor designs for Japanese and European DEMO fusion reactors, *Nucl. Fusion* 61 (2021), 126057.
- [4] G. Federici, et al., *Magnetic Confinement Fusion-Technology-Fusion Core*, Encyclopedia Nuclear Energy, Elsevier (2021) 554–575.
- [5] J.H. You, et al., Divertor of the European DEMO: Engineering and technologies for power exhaust, *Fusion Eng. Des.* 175 (2022), 113010.
- [6] J.H. You, et al., European DEMO divertor target: Operational requirements and material-design interface, *Nucl. Mater. Ener.* 9 (2016) 171–176.
- [7] J.H. You, et al., European divertor target concepts for DEMO: Design rationales and high heat flux performance, *Nucl. Mater. Ener.* 16 (2018) 1–11.
- [8] A. Tincani, et al., Hydraulic characterization of the full scale mock-up of the DEMO divertor outer vertical target, *Energy* 14 (2021) 8086.
- [9] J.H. You, et al., Nuclear loads and nuclear shielding performance of EU DEMO divertor: A preliminary neutronics evaluation of two interim design options, *Nucl. Mater. Ener.* 23 (2020), 100745.
- [10] S. Noce, et al., Nuclear analyses for the design of the ITER-like plasma facing components vertical targets of the DEMO divertor, *Fusion Eng. Des.* 155 (2020), 111730.
- [11] S. Noce, et al., Neutronics analysis and activation calculation for Tungsten used in the DEMO divertor targets: A comparative study between the effects of WCLL and HCPB blanket, different W compositions and Chromium, *Fusion Eng. Des.* 169 (2021), 112428.
- [12] J.H. You, et al., Structural lifetime assessment for the DEMO divertor targets: Design-by-analysis approach and outstanding issues, *Fusion Eng. Des.* 164 (2021), 112203.
- [13] T. Hirai, et al., Use of tungsten material for the ITER divertor, *Nucl. Mater. Ener.* 9 (2016) 616–622.
- [14] J.H. You, et al., High-heat-flux technologies for the European demo divertor targets: State-of-the-art and a review of the latest testing campaign, *J. Nucl. Mater.* 544 (2021), 152670.
- [15] M. Li, et al., Interpretation of the deep cracking phenomenon of tungsten monoblock targets observed in high-heat-flux fatigue tests at 20 MW/m², *Fusion Eng. Des.* 101 (2015) 1–8.
- [16] M. Li, et al., Structural impact of armor monoblock dimensions on the failure behavior of ITER-type divertor target components: Size matters, *Fusion Eng. Des.* 113 (2016) 162–170.
- [17] M. Li, et al., Design options to mitigate deep cracking of tungsten armor, *Fusion Eng. Des.* 124 (2017) 468–472.
- [18] P.A. Di Maio, et al., On the numerical assessment of the thermal-hydraulic operating map of the DEMO divertor plasma facing components cooling circuit, *Fusion Eng. Des.* 161 (2020), 111919.
- [19] P.A. Di Maio, et al., Hydraulic assessment of an upgraded pipework arrangement for the DEMO divertor plasma facing components cooling circuit, *Fusion Eng. Des.* 168 (2021), 112368.
- [20] F. Crescenzi, et al., ITER-like divertor target for DEMO: Design study and fabrication test, *Fusion Eng. Des.* 124 (2017) 432–436.
- [21] E. Visca, et al., Manufacturing and testing of ITER-like divertor plasma facing mock-ups for DEMO, *Fusion Eng. Des.* 136 (2018) 1593–1596.
- [22] M. Richou, et al., Performance assessment of high heat flux W monoblock type target using thin graded and copper interlayers for application to DEMO divertor, *Fusion Eng. Des.* 146 (2019) 858–861.
- [23] M. Richou, et al., Performance assessment of thick W/Cu graded interlayer for DEMO divertor target, *Fusion Eng. Des.* 157 (2020), 111610.
- [24] M. Fursdon et al., The development and testing of the thermal-break divertor monoblock target design delivering 20MW/m² heat load capability, *Phys. Scr.* T170 (2017) 014042 (7pp).
- [25] A. Lukenskas, et al., High heat flux test results for a thermal break DEMO divertor target and subsequent design and manufacture development, *Fusion Eng. Des.* 146 (2019) 1657–1660.
- [26] A.V. Müller et al., Melt infiltrated W-Cu composites as advanced heat sink materials for plasma facing components of future nuclear fusion devices, *Fusion Eng. Des.* 124 (2017) 455–459.
- [27] A.V. Müller et al., Application of tungsten-copper composite heat sink materials to plasma-facing component mock-ups, *Phys. Scr.* T171 (2020) 014015 (8pp).
- [28] J.H. You, et al., Probabilistic failure analysis of a water-cooled tungsten divertor: Impact of embrittlement, *J. Nucl. Mater.* 375 (2008) 283–289.
- [29] M. Li, et al., Fracture mechanical analysis of tungsten armor failure of a water-cooled divertor target, *Fusion Eng. Des.* 89 (2014) 2716–2725.
- [30] K. Zhang, et al., Crack formation in the tungsten armour of divertor targets under high heat flux loads: A computational fracture mechanics study, *Fusion Eng. Des.* 184 (2022), 113305.
- [31] D. Terentyev, et al., Recent progress in the assessment of irradiation effects for in-vessel fusion materials: tungsten and copper alloys, *Nucl. Fusion* 62 (2022), 026045.
- [32] H. Greuner, et al., High heat flux facility GLADIS: Operational characteristics and results of W7-X pre-series target tests, *J. Nucl. Mater.* 367–370 (2007) 1444–1448.
- [33] I. Bobin-Vastra, et al., Activity of the European high heat flux test facility: FE200, *Fusion Eng. Des.* 75–79 (2005) 357–363.
- [34] S. Roccella, et al., Ultrasonic test results before and after high heat flux testing on W-monoblock mock-ups of EU-DEMO vertical target, *Fusion Eng. Des.* 160 (2020), 111886.
- [35] F. Gally et al., Quantitative thermal imperfection definition using non-destructive infrared thermography on an advanced DEMO divertor concept, *Phys. Scr.* T170 (2017) 014015 (5pp).
- [36] G. Dose, et al., Ultrasonic analysis of tungsten monoblock divertor mock-ups after high heat flux test, *Fusion Eng. Des.* 146 (2019) 870–873.
- [37] Y. Addab, et al., Typology of defects in DEMO divertor target mockups, *Phys. Scr.* 96 (2021), 124065.
- [38] T. Minniti, et al., Structural integrity of DEMO divertor target assessed by neutron tomography, *Fusion Eng. Des.* 169 (2021), 112661.
- [39] H. Greuner, et al., Progress in high heat flux testing of European DEMO divertor mock-ups, *Fusion Eng. Des.* 146 (2019) 216–219.
- [40] H. Greuner, et al., Assessment of the high heat flux performance of European DEMO divertor mock-ups, *Phys. Scr.* T171 (2020), 014003.
- [41] M. Li, et al., Structural impact of creep in tungsten monoblock divertor target at 20 MW/m², *Nucl. Mater. Ener.* 14 (2018) 1–7.
- [42] M. Li, et al., Low cycle fatigue behavior of ITER-like divertor target under DEMO-relevant operation conditions, *Fusion Eng. Des.* 90 (2015) 88–96.
- [43] M. Fursdon, et al., Enhancements in the structural integrity assessment of plasma facing components, *Fusion Eng. Des.* 146 B (2019) 1591–1595.
- [44] M. Fursdon, et al., Towards reliable design-by-analysis for divertor plasma facing components - guidelines for inelastic assessment (part I: unirradiated), *Fusion Eng. Des.* 147 (2019), 111234.
- [45] M. Li, et al., Sweeping heat flux loads on divertor targets: thermal benefits and structural impacts, *Fusion Eng. Des.* 102 (2016) 50–58.
- [46] F. Maviglia, et al., Limitations of transient power loads on DEMO and analysis of mitigation techniques, *Fusion Eng. Des.* 109–111 (2016) 1067–1071.
- [47] F. Escourbiac, et al., Assessment of critical heat flux margins on tungsten monoblocks of the ITER divertor vertical targets, *Fusion Eng. Des.* 146 (2019) 2036–2039.
- [48] R. Coppola, et al., Neutron diffraction measurement of residual stresses in an ITER like tungsten-monoblock type plasma-facing component, *Fusion Eng. Des.* 146 (2019) 701–704.
- [49] J.H. You, A review on two previous divertor target concepts for DEMO: Mutual impact between structural design requirements and materials performance, *Nucl. Fusion* 55 (2015), 113026.
- [50] M. Fursdon, et al., Towards reliable design-by-analysis for divertor plasma facing components - Guidelines for inelastic assessment (part II: irradiated), *Fusion Eng. Des.* 160 (2020), 111831.
- [51] ITER structural design criteria for in-vessel components (SDC-IC) appendix A: materials design limit data, G 74 MA 8 01-05-28 W0.2, 2001.
- [52] ITER Material Properties Handbook, ITER Document No. G74 MA16, 2005.
- [53] T. Hirai, et al., Status of technology R&D for the ITER tungsten divertor monoblock, *J. Nucl. Mater.* 463 (2015) 1248–1251.